Dalton Transactions

ROYAL SOCIETY OF CHEMISTRY

PAPER

View Article Online
View Journal | View Issue

Cite this: *Dalton Trans.*, 2023, **52**, 15995

Predicting the dye-sensitized solar cell performance of novel linear carbon chain-based dyes: insights from DFT simulations†

Giuseppe Consiglio, [a] Adam Gorcyński, [b] Salvatore Petralia [c] and Giuseppe Forte *[c]

In this paper, we employ density functional theory (DFT) simulations to predict the energy conversion efficiency of a novel class of organic dyes based on linear carbon chain (LCC) linkers for application in dye-sensitized solar cells (DSSCs). We investigate the role of the anchoring group, which serves as a bridge connecting the linker and the surface. Specifically, we compare the performance of cyanoacrylic acid, dyes **PY-4N** and **PY-3N**, with that of phosphonate derivatives, dyes **PY-4NP** and **PY-3NP**, wherein the carboxylic group of the cyanoacrylic moiety is replaced with phosphonic acid. The observed variations in the UV/VIS absorption spectra have a slight impact on the light harvesting efficiency (LHE). Based on the empirical parameters we have taken into account, the electron injection efficiency (Φ_{inj}) and electron collection efficiency (η_{coll}) values do not impact the short-circuit current density (J_{SC}) values of all the studied dyes. The open-circuit voltage (V_{oc}) is theoretically predicted using the improved normal model (INM) method. Among the dyes, **PY-4N** and **PY-3N** demonstrate the highest V_{oc} values. This can be attributed to a more favorable recombination rate value, which is related to the energy gap between the HOMO level of the dyes and the conduction band minimum (CBM) of the surface. Dyes **PY-4N** and **PY-3N** are predicted to demonstrate remarkably high photoelectric conversion efficiency (PCE) values of approximately 21.79% and 16.52%, respectively, and therefore, they are expected to be potential candidates as organic dyes for applications in DSSCs. It is worth noting that **PY-4NP** and **PY-3NP** exhibit strong adsorption energy on the surface and interesting PCE values of 11.66% and 8.29%, respectively. This opens up possibilities for their application in DSSCs either as standalone sensitizers or as co-sensitizers alongside metal-free organic dyes or organic–inorganic perovskite solar cells.

Received 15th June 2023,
Accepted 2nd October 2023

DOI: 10.1039/d3dt01856c

rsc.li/dalton

1. Introduction

Dye-sensitized solar cells have emerged as a promising technology for efficient conversion of solar energy into electrical power. DSSCs have garnered significant interest due to their low-cost fabrication along with their peculiar optical and mechanical properties, and high device efficiency.[1–3] One of the key components of DSSCs is represented by the photosensitizer, which plays a crucial role in absorbing photons and starting the charge separation process.[4] Over the years, significant research efforts have been dedicated to optimizing the design of dyes with the aim of enhancing the performance of DSSCs. Extensive investigations have been conducted on a wide range of photosensitizers, primarily categorized into three main classes: ruthenium(II) complexes, zinc(II) porphyrin derivatives and metal-free organic dyes. Synthesis and characterization studies have been carried out to explore the potential of these photosensitizers in DSSCs, seeking to improve their efficiency and overall performance.

Ruthenium complexes are frequently employed in DSSC photosensitization due to their favorable characteristics, including a prolonged excited-state lifetime and robust electrochemical stability.[5–7] Within this category of compounds, those featuring dual isocyanate ligands exhibit an absorption profile that extends up to 800 nm, resulting in substantial enhancement in photocurrent density when examined under short-circuit conditions.[8–15] Recent advancements have seen the doping of the most popular derivative N719 with graphene quantum dots. Under excitation illumination, these quantum

[a]Department of Chemical Sciences, University of Catania, Via S. Sofia 64, 95125, Italy
[b]Faculty of Chemistry, Adam Mickiewicz University, Uniwersytetu Poznańskiego 8, 61-614 Poznań, Poland
[c]Department of Drug Sciences and Health, University of Catania, Via S. Sofia 64, 95125, Italy. E-mail: gforte@unict.it

†Electronic supplementary information (ESI) available. See DOI: https://doi.org/10.1039/d3dt01856c

dots emit photons at wavelengths that align with the absorption characteristics of the ruthenium dye within the active layer of the DSSC. This process augments the generation of free electrons in the DSSC structure, consequently increasing the power-conversion efficiency up to 11.27%.[16] In addition, a multitude of strategies have been devised to optimize ruthenium complexes, aiming to increase their molar extinction coefficients and expand their optical absorption capabilities into the NIR.[17] Younas *et al.* employed a co-sensitization approach, using the N749 Ru-based dye in conjunction with the organic sensitizer RK1. This approach yielded an efficiency of 8.15%, surpassing the efficiency achieved by individual dyes.[18] Porphyrin derivatives have demonstrated electron injection properties comparable to those observed in Ru-based DSSCs.[19] Subsequent investigations have unveiled the promising attribute of push–pull porphyrins, a class of compounds characterized by the strategic placement of an electron donor group and an electron acceptor–donor group spaced by the macrocycle. These compounds offer several advantages, including the broadening of the optical absorption range, enhanced light harvesting efficiency (LHE) and improved electron injection characteristics.[20] These findings contributed to the development of numerous push–pull porphyrin derivatives, with the primary objective of further enhancing both efficiency and stability.[21–28]

To enhance the DSSC performance, porphyrins have been employed in co-sensitization quantities with organic dyes. This approach is particularly valuable due to the limited absorption intensity of porphyrins in the 500–600 nm range. Co-sensitization effectively compensates for this deficiency.[29] In an effort to mitigate the undesirable aggregation effect of dyes, a novel class of porphyrin sensitizers, based on phenothiazine as the donor group, has been synthesized. The results have demonstrated improvements in both the open-circuit voltage (V_{oc}) and the short-circuit current density (J_{sc}), ultimately yielding an efficiency of 9.3%.[30] The free-metal class, in particular, has garnered significant attention due to its low-cost fabrication processes. This class primarily consists of three distinct regions with different purposes. First, an electron acceptor moiety (A) anchors the dye to the semiconducting electrode, ensuring an efficient electronic coupling between the sensitizers and the substrate. Second, a linker section (π) comprises a conjugated system that facilitates electron transfer. Finally, an electron donor moiety (D) is located at the free end of the molecule. Thus, these dyes are typically based on a push–pull structure, denoted as D–π–A. Various strategies have been explored to optimize the electron acceptor and electron donor moieties in order to achieve higher efficiency and improved performance in photovoltaic applications. Thieno[3,2-*b*]indole and thieno[3,2-*b*]benzothiophene derivatives have been employed, including in co-sensitization, as new bridge units in D–π–A structured organic dyes, resulting in excellent values of the PCE.[31–35] Triphenylamine-based donor units have found extensive use in photovoltaic applications.[36,37] Moreover, dyes incorporating perylene and phenothiazine moieties have been synthesized to achieve superior attributes, including enhanced stability, cost-effectiveness and efficiency.[38,39] Jiang and co-workers have recently developed novel dyes featuring quinoxaline or quinoxalinoid moieties, resulting in co-sensitized devices attaining an efficiency value exceeding 30% under indoor light conditions.[40] Furthermore, superior performances have been achieved by incorporating rigid aromatic systems in the molecular structure, thereby enhancing planarity and, consequently, facilitating electron flow between donor and acceptor moieties.[41–43] Dyes characterized by an anthracene donor group have demonstrated exceptional efficiency, greater than 20%, under low-light conditions. In addition, these dyes have shown favorable performance when co-sensitized with a porphyrin dye.[44] Promising results have been obtained through the utilization of thiophene and dithiophene derivatives in the π-bridge.[45,46] In the latter case, a notable reduction in dye aggregation has been reported.[47] The introduction of alkynyl bridge groups has been shown to enhance absorption capacity, yielding remarkable J_{sc} values, and, overall, significantly improving the photovoltaic performance.[48–53] High-performing DSSCs commonly feature acceptor-anchoring groups primarily represented by cyanoacrylic and benzoic moieties, which have demonstrated excellent performance in numerous studies; see the references cited above. In recent years, the incorporation of phosphonate groups as bridging units between the dye and TiO_2 electrodes has gained significant attention in the field of DSSC research. The introduction of phosphonate moieties provides excellent stability, and furthermore, introduces additional anchoring points and improves the stability under prolonged exposure to light and electrolyte conditions.[5] Murakami and co-workers synthesized a carbazole-based dye incorporating a phosphonic acid anchor and evaluated its performance in solar cells under thermal stress, comparing it to dyes with a carboxylic acid anchor. The investigation revealed that the presence of the phosphonic acid anchor effectively enhanced the long-term heat stability of the DSSCs. Moreover, the introduction of a strong acceptor group led to a stable and highly efficient dye.[54] However, several studies have shown that cells with a carboxylic acid group result in better performances when compared with phosphonic acid anchor group cells.[55] One of the reasons suggested by Baktash and co-workers behind the lesser performance observed in the phosphonic acid linker family is the significant energy gap between the dye's LUMO and the LUMO of the phosphonic acid linkers, in comparison with carboxyl derivatives. In addition, a decrease in tunneling probability is observed due to the very limited contribution of the oxygen atoms that connect the linker to the surface.[56] It is worth noting that injection time strongly depends on the anchoring mode with fully dissociative bidentate geometries, which are found to have the fastest injection time compared to the other coordination modes.[57] Recently, Vats and co-workers have synthesized novel dye–sensitizers from the squaraine family featuring dual anchoring groups. In particular, the dye that incorporates phosphonic acid and acrylic acid as anchoring groups demonstrates a binding affinity with the surface that is over 500 times stronger than

that of the cyanoacrylic dye, with a minor reduction in the photoelectric conversion efficiency.[58] A DFT study conducted by Fadili *et al.* demonstrated that the addition of a cyano moiety in proximity to the phosphonic acid anchor group enhanced both the absorption properties and the nonlinear optical (NLO) properties of the compound, while also reducing the energy gap.[59] The same research group investigated the impact of auxiliary acceptor groups incorporated into the central region of the dye–sensitizer structure, while maintaining a cyanophosphonic moiety as the anchor. This modification resulted in a broader optical absorption spectrum and exhibited favorable NLO properties.[60] A computational study of copper(I) complexes incorporating phosphonic acid anchor dyes revealed an enhanced LHE and an overall improved photoelectric performance.[61] In a previous computational study, our research focused on examining the photophysical properties of a novel class of organic dyes based on linear carbon chain (LCC) linkers, aiming to explore their potential application in DSSCs.[62] This focus on LCCs stems from their known attributes of high electrical conduction and very unusual optoelectronic behavior.[63–68] Our findings revealed that introduction of a 2-amino pyrrole unit as the donor moiety enhances molecular planarity compared to thiophene derivatives. This increased planarity, in turn, promoted efficient electron transfer between the donor and acceptor moieties, leading to improved performance in terms of LHE and, consequently, J_{sc}. Moreover, insertion of LCC linkers produced substantial effects on the absorption spectra, influencing both the visible and UV regions, and electrochemical properties.[62] Building upon these prior results, the present study delves deeper into the investigation of the photovoltaic properties of the most promising derivatives, specifically **PY-4N** and **PY-3N**, by means of density functional theory (DFT) calculations. In greater detail, we examine the interaction of these dyes with a TiO_2 anatase (101) supercell, which consists of a total of 384 atoms. The results obtained are then used to assess key parameters such as electron injection (k_{inj}), electron recombination (k_{rec}), J_{sc} and V_{oc}. In addition, we explore the photovoltaic characteristics of the dyes obtained by replacing the carboxylic acid moiety with phosphonic acid, as illustrated in Scheme 1. Through this comprehensive study, we aim to gain further insights into the potential advantages offered by both the use of LCC as a π-linker and the incorporation of phosphonic acid as an anchoring group.

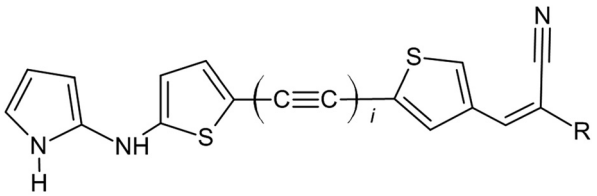

R = COOH i=3 **PY-3N**

R = COOH i=4 **PY-4N**

R = PO_3H_2 i=3 **PY-3NP**

R = PO_3H_2 i=4 **PY-4NP**

Scheme 1 Molecular structures of the designed dyes: **PY-3N** (2*E*)-2-cyano-3-(5-{6-[5-(1*H*-pyrrol-2-ylamino)thiophen-2-yl]hexa-1,3,5-triyn-1-yl}thiophen-3-yl)prop-2-enoic acid; **PY-4N** (2*E*)-2-cyano-3-(5-{8-[5-(1*H*-pyrrol-2-ylamino)thiophen-2-yl]octa-1,3,5,7-tetrayn-1-yl}thiophen-3-yl)prop-2-enoic acid; **PY-3NP** [(*E*)-1-cyano-2-(5-{6-[5-(1*H*-pyrrol-2-ylamino)thiophen-2-yl]hexa-1,3,5-triyn-1-yl}thiophen-3-yl)ethenyl] phosphonic acid; and **PY-4NP** [(*E*)-1-cyano-2-(5-{8-[5-(1*H*-pyrrol-2-ylamino)thiophen-2-yl]octa-1,3,5,7-tetrayn-1-yl}thiophen-3-yl)ethenyl] phosphonic acid.

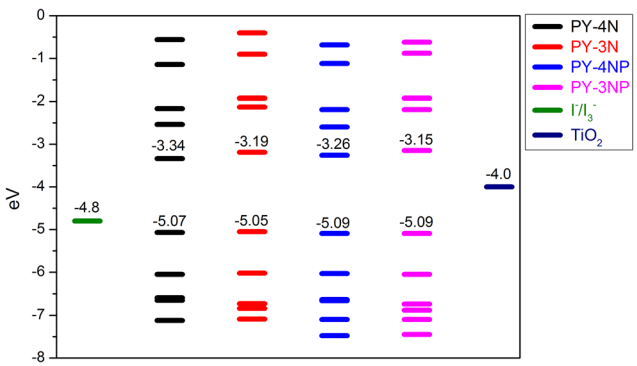

Fig. 1 Selected MO energy levels for the studied dyes in acetonitrile at the B3LYP/6-311+G(3df,3dp)/SMD level. The TiO_2 CB and the redox potential of I^-/I_3^- are reported as reference values.

2. Results and discussion

2.1 UV-Vis absorption and FMO

A basic requirement for dye sensitizers to be potentially used in DSSCs is the appropriate energy level of the LUMO, which facilitates an efficient electron injection into the TiO_2 conduction band (CB). Furthermore, an optimal HOMO energy level is useful for efficient electron collection. Fig. 1 displays the energy diagram of selected molecular orbitals for the studied dyes at the 6-311+G(3df,3pd)/SMD level of theory. It is evident from the diagram that the HOMO levels of all four dyes are located below −4.8 eV, the redox potential value of the I^-/I_3^- electrolyte with respect to the vacuum level,[69] which ensures efficient electron recovery. On the other hand, the LUMO energy levels are significantly higher than the TiO_2 CB, −4.0 eV,[70] enabling rapid injection of excited dye electrons into the semiconductor. The data illustrated in Fig. 1 indicate that substituting the carboxyl group with the phosphonic group yields minimal differences in the HOMO energy levels, whereas modest energy increases are detected for the LUMO energy levels, suggesting potentially higher efficiency in electron injection. For further comparison, PBE and M06 functionals were employed to determine the band gap, and the results (see ESI Table 1)† reveal a similar trend among the molecules. Specifically, PBE and M06 yield larger gap values compared to B3LYP; furthermore, these functionals exhibit HOMO values

lower in energy and LUMO values higher in energy than those obtained with B3LYP. These data suggest greater energy differences between the dye's HOMO and the redox potential of the I^-/I_3^- electrolyte, implying a more efficient electron recovery process. Moreover, the higher LUMO energy levels, which significantly exceeded the TiO_2 CB at −4.0 eV, facilitate the rapid injection of excited dye electrons into the semiconductor.

In general, a wide absorption range and a high absorption intensity of the dye are crucial for achieving good performance as a sensitizer. To this end, UV-Vis absorption spectra were simulated using the CAM-B3LYP functional, which has proven to be highly reliable in predicting experimental absorption spectra of molecules similar to the dyes under investigation (see above).

The simulated absorption spectra are presented in Fig. 2, while the wavelengths, oscillator strength (f) > 0.2, and the main contributions to the transitions are listed in Table 1. As previously observed for **PY-4N** and **PY-3N**, the phosphonate derivatives also exhibit a prominent peak between 500 and 600 nm. This peak corresponds to the HOMO → LUMO transition and is attributed to the intermolecular charge transfer. A slight red shift is found for the more extended π-conjugated systems, *e.g.* **PY-4N** and **PY-4NP**; the overlapped HOMO and LUMO MOs through the linker indicates the excellent induction and electron-withdrawing properties of the donor and acceptor groups (see Fig. 3). In addition, a second absorption band between 300 and 350 nm is present, but its intensity is notably lower in **PY-3N** and **PY-3NP** dyes compared to **PY-4N** and **PY-4NP**, respectively. It is worth noting that such a difference is reflected in the photovoltaic properties, particularly the LHE, and in turn J_{SC}, as illustrated by the data presented in Table 3 and Fig. 5.

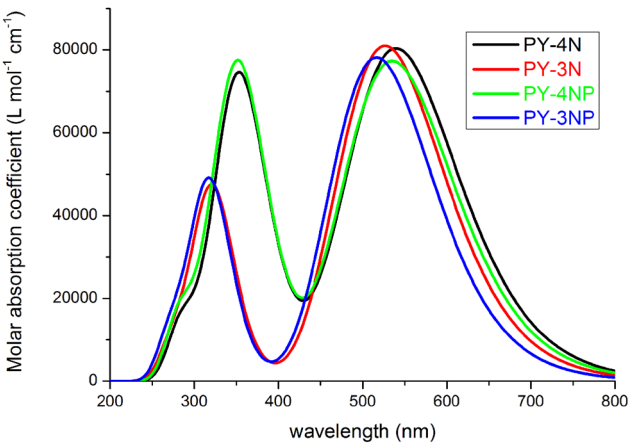

Fig. 2 UV/Vis absorption spectra of dyes in acetonitrile at the TD-CAM-B3LYP/6-311+G(3df,3pd)/SMD level. All the spectra are Gaussian broaded with 0.3 eV (half width half maximum).

Table 1 The absorption wavelengths (nm), oscillator strengths and main contributions to the transitions of dyes in acetonitrile at the CAM-B3LYP/6-311 + G(3df,3pd)/SMD level

Compound	λ	f	Main contributions to the transitions
PY-4N	538.99	1.75	H → L (50%)
	366.70	0.86	H−2 → L+1 (37%)
	343.14	1.09	H → L+2 (30%)
	287.05	0.33	H−3 → L (38%)
PY-3N	526.71	2.00	H → L (68%)
	322.03	1.12	H−3 → L+1 (26%)
	276.57	0.20	H−2 → L (43%)
PY-4NP	534.66	1.85	H → L (56%)
	364.53	1.16	H−2 → L+1 (36%)
	336.87	0.97	H → L+2 (31%)
	283.76	0.23	H−7 → L (48%)
PY-3NP	517.22	1.89	H → L (67%)
	319.64	1.00	H−3 → L+1 (15%)
	273.65	0.24	H−2 → L (31%)

2.2 Adsorption on TiO_2

To investigate the electron transfer process at the interface, we focused on the adsorption complexes of dyes@TiO_2. For all cases, we considered the bidentate bridging mode, which has been reported as the most stable adsorption mode for both carboxylic and phosphonic groups.[70–73] In this model, the sensitizer binds to the semiconductor with two O–Ti bonds, whereas the protonated H atom of the acid group is donated to the nearest double-coordinated surface oxygen atom. The calculated adsorption energies listed in Table 2 indicate strong interactions between the dyes and the surface. Consistent with previous studies, **PY-4NP** and **PY-3NP** exhibit more negative adsorption energies, indicating a stronger interaction with the TiO_2 anatase, compared to compounds bridged with carboxylic acid.[5,74,75] Analyzing the distance between carbon atoms in LCCs reveals alternating values along the chain, with bond lengths ranging from 1.21 to 1.33 Å (see ESI Table 2)† and an approximate average value of 1.26 Å, falling between the values of 1.20 Å for –C≡C– and 1.34 Å for –C=C–. The energy values for HOMO and LUMO presented in Table 2 also suggest a potential approach to a limit of the LCC chain length, beyond which there is not a significant reduction in the band gap. As the LCC increases, a deviation from linearity may hinder electron transfer from the donor to the acceptor, thus impacting the photovoltaic performance. Fig. 4 presents the partial density of states (PDOS) for the interfaces of dyes@TiO_2. As observed, the calculated LUMO energy levels of all the sensitizers are located above the conduction band minimum of TiO_2, ensuring an efficient driving force for the electron transfer to the semiconductor's CB, as shown in Table 2 ($\Delta G^{\circ}_{inject}$).

However, the LUMO energy values in the phosphonate-based dyes remain essentially unchanged after adsorption, whereas those of the cyanoacrylate derivatives shift to higher values, ensuring more efficient electron injection. HOMO energy levels are lower in energy compared to the electrolyte redox potential, thus guaranteeing favorable ground-state dye regeneration (ΔG°_{rec}). In this case, the HOMO energy level shifts to lower values upon adsorption for cyanoacrylic derivatives, ensuring significantly efficient recombination rates compared to those of the phosphonate derivatives. This results in a significant enhancement in the V_{oc} values for **PY-4N** and **PY-3N**, consequently improving their overall performance, as

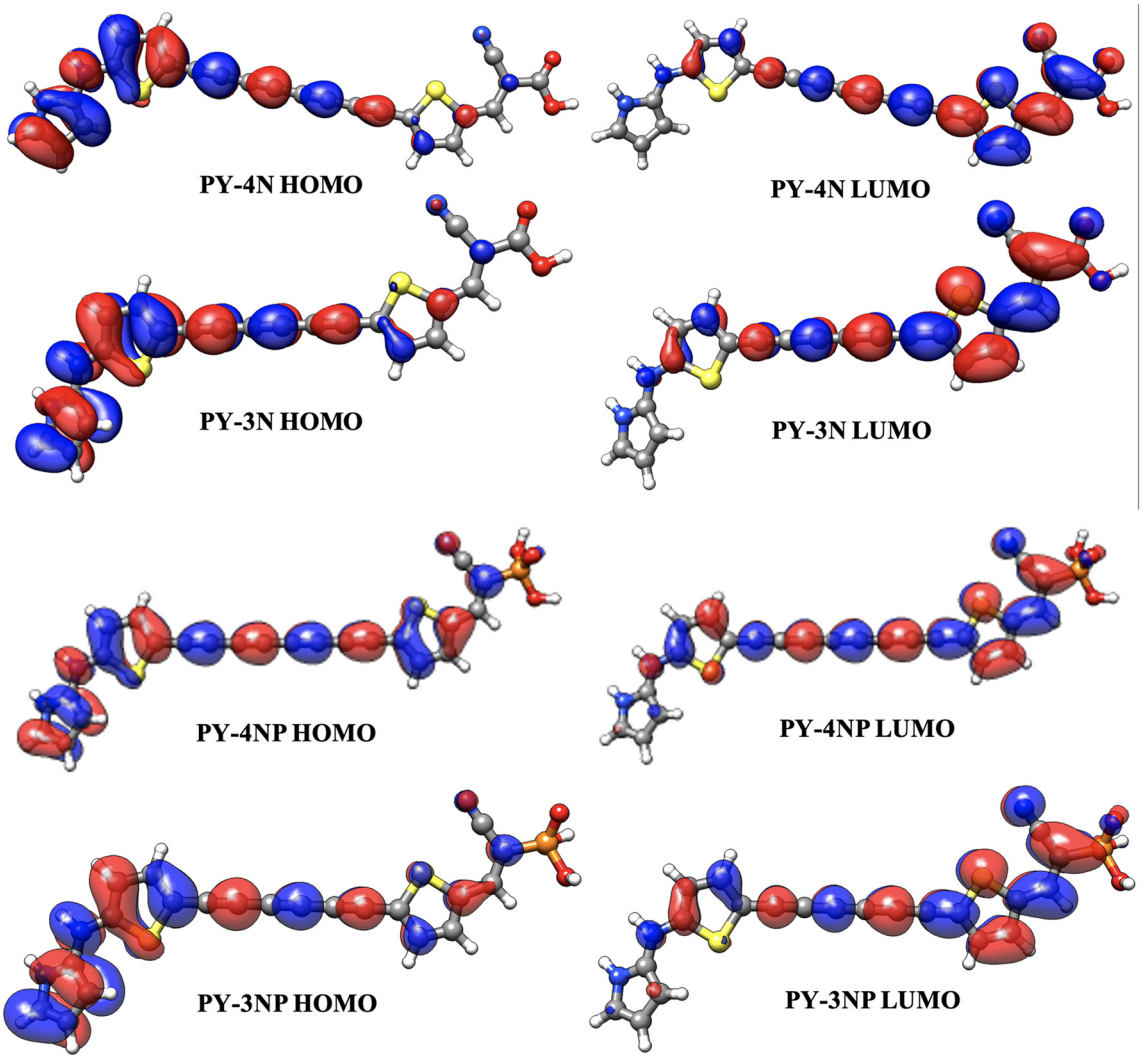

Fig. 3 Frontier molecular orbitals of the dyes in acetonitrile at the TD-CAM-B3LYP/6-311+G(3df,3dp)/SMD level.

Table 2 Adsorption energies, energy levels and driving forces calculated for dyes@TiO_2. All the energies are in eV

Compound	E_{ads} [a]	HOMO	LUMO	CBM	$\Delta G^{\circ}_{inject}$ [b]	ΔG°_{rec} [c]
PY-4N@TiO_2	0.89	−5.23	−2.91	−3.52	0.61	1.71
PY-3N@TiO_2	0.88	−5.23	−2.84	−3.54	0.70	1.69
PY-4NP@TiO_2	3.06	−5.14	−3.12	−3.56	0.44	1.58
PY-3NP@TiO_2	3.06	−5.11	−3.10	−3.57	0.47	1.54

[a] $E_{ads} = E_{Dye@TiO_2} - (E_{TiO_2} + E_{Dye})$. [b] $\Delta G^{\circ}_{inj} = E_{LUMO} - E_{CBM}$. [c] $\Delta G^{\circ}_{rec} = E_{CBM} - E_{HOMO}$.

discussed below. To confirm this prediction, we focused on calculating the photoelectric conversion efficiency.

2.3 Photovoltaic properties

The photoelectronic conversion efficiency (η) of the solar cell device can be expressed as follows:[76]

$$\eta = \frac{J_{SC} \cdot V_{OC}}{P_{in}} \cdot FF$$

where P_{in} is the incident solar power on the cell and FF is the fill factor. In a DSSC, the short-circuit photocurrent can be evaluated as:[77]

$$J_{SC} = q \int LHE(\lambda)\Phi_{inj}\eta_{reg}\eta_{coll}\vartheta_{ph.AM1.5G}(\lambda)d\lambda$$

where q is the elementary charge of the electron, and Φ_{inj} represents the electron injection efficiency, which is defined as:[21]

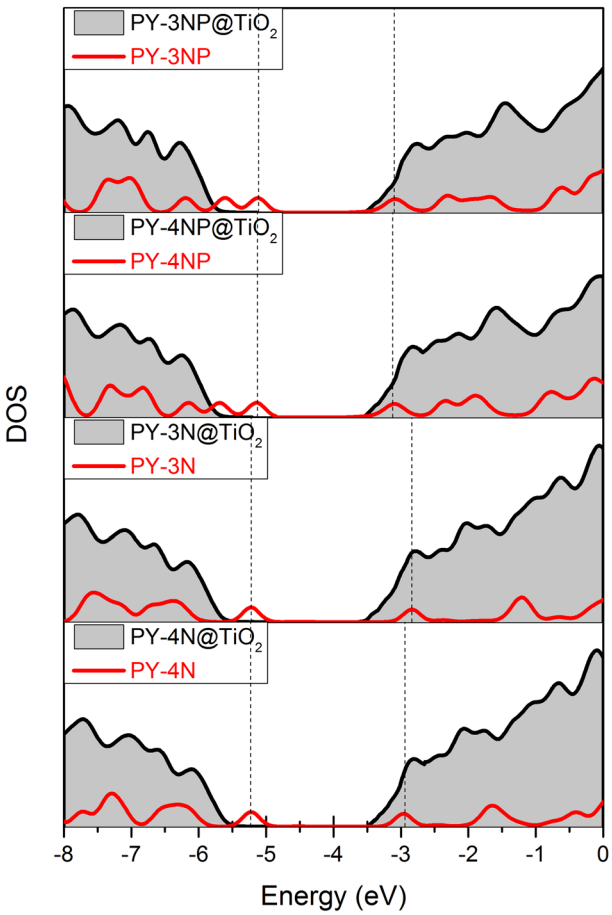

Fig. 4 Calculated PDOS for **PY-4N**, **PY-3N**, **PY4NP** and **PY-3NP**. Dashed lines refer to the HOMO and LUMO energy levels.

$$\Phi_{\text{inj}} = \frac{1}{\left(1 + \frac{\tau_{\text{inj}}}{\tau_{\text{relax}}}\right)}$$

where η_{reg} is the dye regeneration efficiency, which is set equal to 1, and η_{coll} is the electron collection efficiency, expressed as:[78]

$$\eta_{\text{coll}} = \frac{1}{\left(1 + \frac{\tau_{\text{trans}}}{\tau_{\text{rec}}}\right)}$$

where $\vartheta_{\text{ph.AM 1.5G}}$ is the photon flux under AM 1.5G solar spectra irradiance. The J_{SC} value is one of the most important factors determining the overall cell efficiency, depending on the light harvesting efficiency, which, in turn, is related to the dye absorption region through the following formula:[79]

$$\text{LHE}\ (\lambda) = 1 - 10^{-\varepsilon(\lambda)\Gamma},$$

where $\varepsilon(\lambda)$ is the molar absorption coefficient at a certain wavelength, whereas Γ is the surface loading of the dye, which is calculated as the product of the dye concentration c with TiO_2 film thickness b. The simulated LHE curves for all dyes are shown in Fig. 5 and the calculated electrochemical parameters are presented in Table 3.

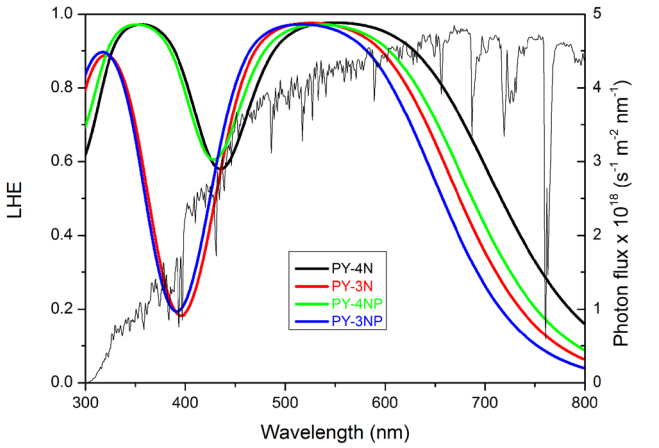

Fig. 5 LHE curves of all dyes (Γ = 20 nmol cm^{-2} is taken for all dyes). The AM 1.5G solar spectrum is reported in grey.

By assuming a time of 10 ps for both the relaxation lifetime of the dye's excited states (τ_{relax}) and the electron-transport time from the CB of the semiconductor to the electrode (τ_{trans}), Φ_{inj} and η_{coll} values are set equal to 1. The inverses of $k_{\text{inj/rec}}$ represent the respective time constant $\tau_{\text{inj/rec}}$.

It is worth noting that significant differences are observed for k_{rec}; however, considering the empirical parameters discussed earlier and the intrinsic limitations of the simulation method, these differences do not have any influence on J_{sc} as both Φ_{inj} and η_{coll} are equal to 1.

Among the studied dyes, the predicted J_{sc} values follow the order **PY-4N** > **PY-4NP** > **PY-3N** > **PY-3NP**. These results are indicative of the overlap between the UV/Vis absorption spectra of the sensitizers and solar spectra irradiance, and thus, dyes with longer π-conjugated LCCs are likely to provide higher efficiency in DSSC applications. Another crucial factor that significantly impacts the overall cell efficiency is represented by V_{oc}, which is defined as the difference between the electrolyte redox potential and the quasi-Fermi level of electrons in the semiconductor. An accurate evaluation of this quantity can be achieved using the improved normal model (INM). This model takes into account the effects of charge recombination as well as several parameters related to device fabrication, such as the electrolyte concentration and the film thickness. Following this approach, V_{oc} can be calculated as:[80]

$$V_{\text{OC}} = \frac{k_{\text{B}}T}{\beta' q} \ln \frac{\beta' q R_0 J_{\text{SC}}}{k_{\text{B}}T}$$

where k_{B} is the Boltzmann constant, T the absolute temperature, β' the charge transfer coefficient for the recombination of the electrons (here, we considered an empirical value of 0.5), and R_0 the recombination resistance, measured in Ω cm^2, and defined as:

$$R_{\text{O}} = \frac{\sqrt{\pi\lambda k_{\text{B}}T}}{q^2 d\gamma k_{\text{rec}} M_{\text{ox}} N_S} \exp\left(\gamma \frac{E_{\text{CBM}} - E_{\text{redox}}}{k_{\text{B}}T} + \frac{\lambda}{4k_{\text{B}}T}\right)$$

where d represents the film thickness (here, we considered an experimental value of 10^{-3} cm);[81] M_{ox} refers to the molarity of the

Table 3 Calculated values of reorganization energy λ (eV), electron injection, r_{inj}, and electron recombination, r_{rec}, distance (Å), electron injection, k_{inj}, and electron recombination, k_{rec}, rates (s^{-1}), short-circuit photocurrent density J_{SC} (mA cm^{-2}), open-circuit voltage V_{oc} (mV), fill factor FF, and photoelectric conversion efficiency η (%)

Compound	λ	r_{inj}	r_{rec}	k_{inj}	k_{rec}	J_{SC}	V_{oc}	FF	η
PY-4N@TiO_2	0.622	2.55	20.12	1.48×10^{14}	2.24×10^{2}	21.08	1156	0.89	21.29
PY-3N@TiO_2	0.606	2.53	18.85	1.31×10^{14}	5.01×10^{2}	17.22	1083	0.89	16.52
PY-4NP@TiO_2	0.751	2.89	21.71	3.28×10^{13}	3.08×10^{6}	19.50	704	0.85	11.66
PY-3NP@TiO_2	0.766	2.89	19.43	3.73×10^{13}	1.82×10^{7}	16.20	605	0.85	8.29

electrolyte oxidized species, with I_3^- set to 0.05 in this case; N_s represents the total number of surface states contributing to the recombination, set to 10^{-5}; the parameter γ was chosen as 0.3 based on the typical experimental data;[82,83] E_{CBM} is the TiO_2 conduction band minimum, while E_{redox} denotes the electrolyte redox potential; and λ corresponds to the sum of the hole and electron reorganization energies ($\lambda_h + \lambda_e$), which are assumed to be the same for both injection and reorganization and are calculated as:[84]

$$\lambda_e = (E_0^- - E_-) + (E_-^0 - E_0)$$

$$\lambda_h = (E_0^+ - E_+) + (E_+^0 - E_0)$$

In this context, $E_0^{+/-}$ represents the energies of the cation and anion obtained from the geometry of the optimized neutral molecule, $E_{+/-}$ refers to the energies of the cation and anion calculated on the basis of the optimized cation and anion, $E^0{}_{+/-}$ are the energies of the neutral molecule calculated from the optimized cation and anion, and E_0 corresponds to the energy of the neutral dye molecule in its ground state. According to the Marcus theory, k_{rec} and k_{inj} are defined as follows:[85]

$$k_{inj/rec} = A\sqrt{\frac{\pi}{\hbar^2 \lambda k_B T}}\ \exp(-\beta r)\exp\left(\frac{-(-\Delta G^{\circ}_{inj/rec} + \lambda)^2}{4\lambda k_B T}\right),$$

where $A = 2.5 \times 10^{-2}$, β is the attenuation factor, set to 0.5, and r is the electron transfer distance.

During the injection process, there is an electron transfer from the dye's LUMO to the semiconductor surface, where the distance between the acid anchoring group of the dye and the TiO_2 surface is represented by r_{inj}. Conversely, in the recombination process, there is an electron transfer from the TiO_2 conduction band to the dye's HOMO, and r_{rec} denotes the distance between the donor group of the dye and the semiconductor.

According to the improved normal model, **PY-4N** exhibits the slowest charge recombination rate, resulting in the highest predicted V_{oc} value (1156 mV) for this dye, followed by **PY-3N** with a value of 1086 mV. **PY-4NP** and **PY-3NP** show a recombination rate constant approximately five orders of magnitude higher, leading to significantly reduced V_{oc} values, specifically, 704 mV for **PY-4NP** and 605 mV for **PY-3NP**. By knowing J_{SC} and V_{oc}, we have obtained the photocurrent–photovoltage (J–V) curve for the considered dyes, as illustrated in Fig. 6. Subsequently, we have calculated the photoelectric conversion efficiency η.

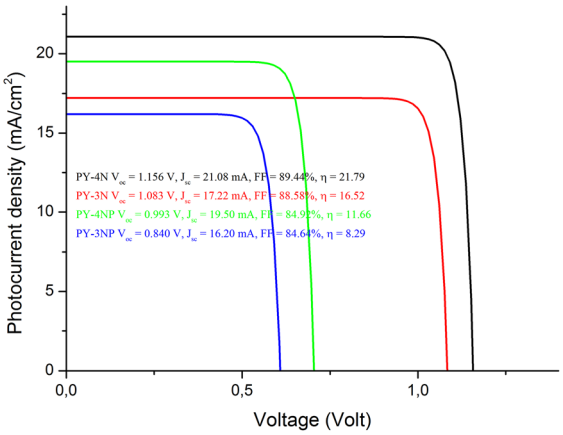

Fig. 6 Calculated J–V curves using the improved normal mode.

The J–V curve was obtained using the following equations:[73,86]

$$J = J_s \cdot \left(1 - e^{\frac{V}{K_B T}}\right) + J_{sc}$$

$$J_s = \frac{J_{sc}}{e^{\frac{qV_{oc}}{K_B T}} - 1}$$

where J_s represents the reverse saturation current. As shown in Fig. 6, we determined the fill factor (FF) of the dyes by calculating the ratio $V_{MAX} \times I_{MAX}/(V_{oc} \times J_{sc})$, where V_{MAX} and I_{MAX} are the maximum voltage and current, respectively.

Cyanoacrylic derivatives demonstrate excellent performances, with η values of 21.29% for **PY-4N** and 16.52% for **PY-3N**. These dyes possess peculiar geometries resulting in significantly large surface coverage. In contrast, **PY-4NP** and **PY-3NP** demonstrate lower efficiency (ranging from 39% and 55%) compared to cyanoacrylic-based dyes, resulting in reduced overall solar cell performance. Specifically, we calculated η values of 11.84% for **PY-4NP** and 9.43% for **PY-3NP**.

However, the results obtained from phosphonate derivatives are particularly intriguing due to the excellent anchoring stability provided by the phosphonate group, surpassing that of cyanoacrylate derivatives.

3. Conclusions

DFT calculations were performed to investigate the photoelectric properties of four organic dyes, each featuring an identical

donor group. The dyes differed in the length of the linear carbon chain serving as a π-linker, with two variations: C_6 and C_8. In addition, the dyes possessed distinct acceptor-anchoring groups: cyanoacrylic (**PY-4N** and **PY-3N**) and phosphonic (**PY-4NP** and **PY-3NP**) moieties. The introduction of the phosphonate group had a marginal effect on the absorption properties, resulting in a slightly lower intensity absorption in the UV range compared to dyes with cyanoacrylic moieties. This, in turn, had a minor effect on the light harvesting efficiency. Injection efficiency and electron collection efficiency values, determined using empirical parameters, were found to be equal to 1, thus having no effect on the J_{SC} values. Dyes **PY-4NP** and **PY-3NP** revealed larger energy differences between the HOMO level and the ECBM, influencing the combination rate constant and resulting in lower V_{oc} values compared to the cyanoacrylic-based dyes. **PY-4N** and **PY-3N** demonstrated remarkable values of 21.29% and 16.52% for the photoelectric conversion efficiency, respectively; moreover, they are expected to efficiently occupy the semiconductor surface. These characteristics make **PY-4N** and **PY-3N** promising candidates for DSSCs. On the other hand, **PY-4NP** and **PY-3NP** exhibited the highest energy adsorption on the surface and displayed lower, but still significant, PCE values of 11.66% and 8.29%, respectively. These findings suggest their potential use as standalone sensitizers or co-sensitizers in photovoltaic applications.

4. Computational methods

The geometries of all dyes were fully optimized in the framework of the density functional theory using the B3LYP functional. A quantitative accuracy level of approximation was achieved by employing the extended basis set 6-311+G(3df,3pd). The vibrational analysis performed on all the investigated structures provided no imaginary modes. To measure the UV/Vis spectra, the TD-DFT approach was employed considering the lowest 10 energy states. As previously demonstrated, the CAM-B3LYP functional yielded results that exhibited good agreement with the experimental data for similar compounds.[62,87,88] It is worth noting that the molecules investigated in this paper are not currently available experimentally, and, as a result, there are no experimental data available for comparison. To account for the solvation effect, the solvated model based on density (SMD) was utilized. All the aforementioned calculations were carried out using the Gaussian 16 package, and the Multiwfn 3.8 program[89] was used to display the molecular orbitals (MOs).

The adsorption process of dyes onto the TiO_2 surface was modeled with a vacuum slab obtained from a 2 × 2 × 4 TiO_2 anatase (101) supercell containing a total of 384 atoms. The dyes were placed orthogonally to the surface, and a 1 nm vacuum region was included above the dye to minimize interactions with the periodic image. As a result, the simulation cell measured 3.87 × 1.51 × 4.75 nm^3 (see Fig. 7). The structures were optimized by using the general gradient approximation, with the Perdew–Burke–Ernzerhof functional employed to approximate the electron exchange and correlation effects. The geometry optimization

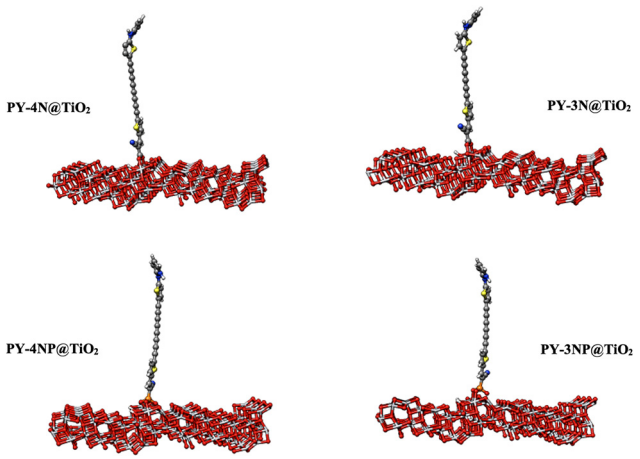

Fig. 7 Geometries of the bidentate binding mode of the dyes on TiO_2.

was performed using the BFGS minimization algorithm and the self-consistent option was chosen for dipole correction. Convergence criteria were set with an energy cutoff of 500 eV and a maximum force of 0.05 eV $Å^{-1}$ for each atom.

The dyes were linked to the TiO_2 surface by bonding the two oxygen atoms of the acid group (carboxylic and phosphonic) to two titanium atoms. This choice is supported by previous studies that have demonstrated the bidentate mode as the most stable binding geometry.[57,60,70,71]

All the calculations on the dyes@TiO_2 systems were performed using the quantum mechanics-based program CASTEP included in the Material Studio package.

Author contributions

Giuseppe Consiglio: conceptualization, investigation, writing, revision and editing. Adam Gorcyński: investigation, writing, revision and editing. Salvatore Petralia: investigation, writing, revision and editing. Giuseppe Forte: conceptualization, supervision, methodology, and writing – original draft.

Conflicts of interest

The authors declare no conflicts of interest.

Acknowledgements

This research was partially funded by the University of Catania (Piano della Ricerca di Ateneo, Linea di Intervento 2, 2018–2020 and the PIACERI – GRABIO project).

References

1 B. O'Regan and M. Grätzel, *Nature*, 1991, **353**, 737–740.
2 M. L. Parisi, S. Maranghi and R. Basosi, *Renewable Sustainable Energy Rev.*, 2014, **39**, 124–138.

3 X. Zhou, Y. Zhang, A. L. Porter, Y. Guo and D. Zhu, *Scientometrics*, 2014, **100**, 705–721.
4 S. Shalini, R. Balasundaraprabhu, T. Satish Kumar, N. Prabavathy, S. Senthilarasu and S. Prasanna, *Int. J. Energy Res.*, 2016, **40**, 1303–1320.
5 A. Hagfeldt, G. Boschloo, L. Sun, L. Kloo and H. Pettersson, *Chem. Rev.*, 2010, **110**, 6595–6663.
6 J. Gong, K. Sumathy, Q. Qiao and Z. Zhou, *Renewable Sustainable Energy Rev.*, 2017, **68**, 234–246.
7 K. Sharma, V. Sharma and S. S. Sharma, *Nanoscale Res. Lett.*, 2018, **13**, 1–46.
8 M. K. Nazeeruddin, P. Péchy and M. Grätzel, *Chem. Commun.*, 1997, **1705**, 1705–1706.
9 M. K. Nazeeruddin, P. Péchy, T. Renouard, S. M. Zakeeruddin, R. Humphry-Baker, P. Comte, P. Liska, L. Cevey, E. Costa, V. Shklover, L. Spiccia, G. D. Deacon, C. A. Bignozzi and M. Grätzel, *J. Am. Chem. Soc.*, 2001, **123**, 1613–1624.
10 R. Buscaino, C. Baiocchi, C. Barolo, C. Medana, M. Grätzel, M. K. Nazeeruddin and G. Viscardi, *Inorg. Chim. Acta*, 2008, **361**, 798–805.
11 Z. Z. Lu, J. Peng, W. De, C. H. Lin, C. G. Wu, K. C. Ho, Y. C. Lin and K. L. Lu, *Eur. J. Inorg. Chem.*, 2016, **8**, 1214–1224.
12 J. F. Huang, J. M. Liu, P. Y. Su, Y. F. Chen, Y. Shen, L. M. Xiao, D. B. Kuang and C. Y. Su, *Electrochim. Acta*, 2015, **174**, 494–501.
13 C. Y. Chen, M. Wang, J. Y. Li, N. Pootrakulchote, L. Alibabaei, C. H. Ngocle, J. D. Decoppet, J. H. Tsai, C. Grätzel, C. G. Wu, S. M. Zakeeruddin and M. Grätzel, *ACS Nano*, 2009, **3**, 3103–3109.
14 F. Gao, Y. Wang, D. Shi, J. Zhang, M. Wang, X. Jing, R. Humphry-Baker, P. Wang, S. M. Zakeeruddin and M. Grätzel, *J. Am. Chem. Soc.*, 2008, **130**, 10720–10728.
15 F. Sauvage, J. D. Decoppet, M. Zhang, S. M. Zakeeruddin, P. Comte, M. Nazeeruddin, P. Wang and M. Grätzel, *J. Am. Chem. Soc.*, 2011, **133**, 9304–9310.
16 A. Barar and D. Manaila-Maximean, *UPB Sci. Bull. A: Appl. Math. Phys.*, 2021, **83**, 309–316.
17 A. Carella, F. Borbone and R. Centore, *Front. Chem.*, 2018, **6**, 481.
18 M. Younas and K. Harrabi, *Sol. Energy*, 2020, **203**, 260–266.
19 Y. Tachibana, S. A. Haque, I. P. Mercer, J. R. Durrant and D. R. Klug, *J. Phys. Chem. B*, 2000, **104**, 1198–1205.
20 Y. C. Chang, C. L. Wang, T. Y. Pan, S. H. Hong, C. M. Lan, H. H. Kuo, C. F. Lo, H. Y. Hsu, C. Y. Lin and E. W. G. Diao, *Chem. Commun.*, 2011, **47**, 8910–8912.
21 A. Yella, H. W. Lee, H. N. Tsao, C. Yi, A. K. Chandiran, M. K. Nazeeruddin, E. W. G. Diau, C. Y. Yeh, S. M. Zakeeruddin and M. Grätzel, *Science*, 2011, **334**, 629–634.
22 S. Mathew, A. Yella, P. Gao, R. Humphry-Baker, B. F. Curchod, N. Ashari-Astani, I. Tavernelli, U. Rothlisberger, M. K. Nazeeruddin and M. Grätzel, *Nat. Chem.*, 2014, **6**, 242–247.
23 G. Consiglio, S. Failla, C. G. Fortuna, L. D'Urso and G. Forte, *Comput. Theor. Chem.*, 2015, **1067**, 1–6.
24 I. P. Oliveri, G. Forte, G. Consiglio, S. Failla and S. Di Bella, *Inorg. Chem.*, 2017, **56**, 14206–14213.
25 S. Aghazada, P. Gao, A. Yella, G. Marotta, T. Moehl, J. Teuscher, J. E. Moser, F. De Angelis, M. Grätzel and M. K. Nazeeruddin, *Inorg. Chem.*, 2016, **55**, 6653–6659.
26 N. V. Krishna, J. V. S. Krishna, M. Mrinalini, S. Prasanthkumar and L. Giribabu, *ChemSusChem*, 2017, **10**, 4668–4689.
27 C. C. Chen, J. S. Chen, V. S. Nguyen, T. C. Wei and C. Y. Yeh, *Angew. Chem., Int. Ed.*, 2021, **60**(9), 4886–4893.
28 S. Mathew, A. Yella, P. Gao, R. Humphry-Baker, F. E. CurchodBasile, N. Ashari-Astani, I. Tavernelli, U. Rothlisberger, K. NazeeruddinMd and M. Grätzel, *Nat. Chem.*, 2014, **6**, 242.
29 H. L. Jia, Y. C. Chen, L. Ji, L. X. Lin, M. Y. Guan and Y. Yang, *Dyes Pigm.*, 2019, **163**, 589–593.
30 K. Zeng, Y. Lu, W. Tang, S. Zhao, Q. Liu, W. Zhu, H. Tian and Y. Xie, *Chem. Sci.*, 2019, **10**, 2186–2192.
31 Y. K. Eom, I. T. Choi, S. H. Kang, J. Lee, J. Kim, M. J. Ju and H. K. Kim, *Adv. Energy Mater.*, 2015, **5**, 1500300.
32 J. M. Ji, H. Zhou, Y. K. Eom, C. H. Kim and H. K. Kim, *Adv. Energy Mater.*, 2020, **10**, 2000124.
33 Y. K. Eom, S. H. Kang, I. T. Choi, Y. Yoo, J. Kim and H. K. Kim, *J. Mater. Chem. A*, 2017, **5**, 2297–2308.
34 J. M. Ji, H. Zhou and H. K. Kim, *J. Mater. Chem. A*, 2018, **6**, 14518–14545.
35 J. M. Ji, H. J. Lee, H. Zhou, Y. K. Eom, C. H. Kim and H. K. Kim, *ACS Appl. Mater. Interfaces*, 2022, **14**(47), 52745–52757.
36 M. Xu, S. Wenger, H. Bala, D. Shi, R. Li, Y. Zhou, S. M. Zakeeruddin, M. Grätzel and P. Wang, *J. Phys. Chem. C*, 2009, **113**, 2966–2973.
37 S. Ahmad, E. Guillén, L. Kavan, M. Grätzel and M. K. Nazeeruddin, *Energy Environ. Sci.*, 2013, **6**, 3439–3466.
38 I. Ouared, M. Rekis and M. Trari, *Dyes Pigm.*, 2021, **190**, 109330.
39 J. Wang, H. Wu, L. Jin, J. Zhang, Y. Yuan and P. Wang, *ChemSusChem*, 2017, **10**, 2962–2967.
40 M. L. Jiang, J. J. Wen, Z. M. Chen, W. H. Tsai, T. C. Lin, T. J. Chow and Y. J. Chang, *ChemSusChem*, 2019, **12**, 3654–3665.
41 S. Chaurasia, C. J. Liang, Y. S. Yen and J. T. Lin, *J. Mater. Chem. C*, 2015, **3**, 9765–9780.
42 J. Wang, H. Wu, L. Jin, J. Zhang, Y. Yuan and P. Wang, *ChemSusChem*, 2017, **10**, 2962–2967.
43 H. Roohi and N. Mohtamadifar, *RSC Adv.*, 2022, **12**, 11557–11573.
44 K. S. K. Reddy, Y. C. Chen, C. C. Wu, C. W. Hsu, Y. C. Chang, C. M. Chen and C. Y. Yeh, *Appl. Mater. Interfaces*, 2018, **10**, 2391–2399.
45 W. H. Liu, I. C. Wu, C. H. Lai, C.-H. Lai, P. T. Chou, Y. T. Li, C. L. Chen, Y. Y. Hsu and Y. Chi, *Chem. Commun.*, 2008, **41**, 5152–5154.
46 C. Bonaccorso, F. De Rossi, M. Panigati, C. G. Fortuna, G. Forte, T. M. Brown, G. M. Farinola and G. Musumarra, *Tetrahedron*, 2015, **71**, 7260–7266.

47 Y. Gao, X. Li, Y. Hu, Y. Fan, J. Yuan, N. Robertson, J. Hua and S. R. Marder, *J. Mater. Chem. A*, 2016, **4**, 12865–12877.
48 B. Nagarajan, S. Kushwaha, R. Elumalai, S. Mandal, K. Ramanujam and D. Raghavachari, *J. Mater. Chem. A*, 2017, **5**, 10289–10300.
49 M. C. Tsai, C. L. Wang, C. W. Chang, C. W. Hsu, Y. H. Hsiao, C. L. Liu, C. C. Wang, S. Y. Lin and C. Y. Lin, *J. Mater. Chem. A*, 2018, **6**, 1995.
50 M. C. Tsai, Y. C. Chiu, M. DeLu, Y. L. Tung, H. C. Tsai, J. R. Chang Chien and C. Y. Lin, *ACS Appl. Energy Mater.*, 2020, **3**, 2744.
51 M. Al-Eid, S. Lim, K. W. Park, B. Fitzpatrick, C. H. Han, K. Kwak, J. Hong and G. Cooke, *Dyes Pigm.*, 2014, **104**, 197–203.
52 D. Wang, H. Han, H. Gao, Z. Yang, Y. Xing, H. Cao, W. He, H. Wang, J. Gu and H. Hu, *Synth. Met.*, 2016, **220**, 41–47.
53 S. S. M. Fernandes, I. Mesquita, L. Andrade, A. Mendes, L. L. G. Justino, H. D. Burrows and M. M. M. Raposo, *Org. Electron.*, 2017, **49**, 194–205.
54 T. N. Murakami, E. Yoshida and N. Koumura, *Electrochim. Acta*, 2014, **131**, 174–183.
55 G. Guerrero, J. G. Alauzun, M. Granier, D. Laurencin and P. H. Mutin, *Dalton Trans.*, 2013, **42**, 12569–12585.
56 A. Baktash, B. Khoshnevisan, A. Sasani and K. Mirabbaszadeh, *Org. Electron.*, 2016, **33**, 207–212.
57 L. Zhang and J. M. Cole, *ACS Appl. Mater. Interfaces*, 2015, **7**, 3427–3455.
58 A. K. Vats, P. Roy, L. Tang, S. Hayase and S. S. Pandey, *Front. Chem. Sci. Eng.*, 2022, **16**(7), 1060–1078.
59 D. Fadili, S. M. Bouzzine and M. Hamidi, *J. Comput. Electron.*, 2020, **19**, 1629–1644.
60 D. Fadili, Z. M. E. Fahim, S. M. Bouzzine, O. T. Alaoui and M. Hamidi, *Comput. Theor. Chem.*, 2022, **1210**, 113645.
61 Q. Zhang, S. Wei, S. Zhou, X. Wei, Z. Xu, Z. Wang, B. Wei and X. Lu, *ACS Appl. Electron. Mater.*, 2020, **2**, 2141–2150.
62 G. Consiglio, A. Gorcyński, S. Petralia and G. Forte, *RSC Adv.*, 2023, **6**(1), 358–369.
63 G. Forte, L. D'Urso, E. Fazio, S. Patanè, F. Neri, O. Puglisi and G. Compagnini, *Appl. Surf. Sci.*, 2013, **272**, 76–81.
64 E. Fazio, L. D'Urso, G. Consiglio, A. Giuffrida, G. Compagnini, O. Puglisi, S. Patanè, F. Neri and G. Forte, *J. Phys. Chem. C*, 2014, **118**, 28812–28819.
65 P. Marabotti, A. Milani, A. Lucotti, L. Brambilla, M. Tommasini, C. Castiglioni, P. Mecik, B. Pigulski, S. Szafert and C. S. Casari, *Carbon Trends*, 2021, **5**, 100115.
66 S. Eisler, A. D. Slepkov, E. Elliott, T. Luu, R. McDonald, F. A. Hegmann and R. Tykwinski, *J. Am. Chem. Soc.*, 2005, **127**, 2666–2676.
67 G. Consiglio and G. Forte, *Phys. Chem. Chem. Phys.*, 2018, **20**, 29754–29763.
68 C. S. Casari, M. Tommasini, R. R. Tykwinski and A. Milani, *Nanoscale*, 2016, **8**, 4414–4435.
69 J. Preat, A. Hagfeldt and E. A. Perpete, *Energy Environ. Sci.*, 2011, **4**, 4537–4549.
70 C. O'Rourke and D. Bowler, *J. Phys.: Condens.Matter*, 2014, **26**, 195302.
71 M. Wagstaffe, A. G. Thomson, M. J. Jackman, M. Torres-Molina, K. L. Syres and K. Handrup, *J. Phys. Chem. C*, 2016, **120**(3), 1693–1700.
72 M. K. Nazeeruddin, R. Humphry-Baker, P. Liska and M. Grätzel, *J. Phys. Chem. B*, 2003, **107**, 8981–8987.
73 K. Srinivas, K. Yesudas, K. Bhanuprakash, V. J. Rao and L. Giribabu, *J. Phys. Chem. C*, 2009, **113**, 20117–20126.
74 P. Pechy, F. P. Rotzinger, M. K. Nazeeruddin, O. Khole, S. M. Zakeeruddin, R. Humphry-Baker and M. Grätzel, *J. Chem. Soc., Chem. Commun.*, 1995, 65–66.
75 M. Nilsing, P. Persson, S. Lunell and L. Ojamae, *J. Phys. Chem. C*, 2007, **111**, 12116–12123.
76 M. Grätzel, *Acc. Chem. Res.*, 2009, **42**, 1788–1798.
77 J. W. Ondersma and T. W. Hamann, *Coord. Chem. Rev.*, 2013, **257**, 1533–1543.
78 S. Haid, M. Marszalek, A. Mishra, M. Wielopolski, J. Teuscher, J. E. Moser, R. Humphry-Baker, S. M. Zakeeruddin, M. Grätzel and P. Baurle, *Adv. Funct. Mater.*, 2012, **22**, 1291–1302.
79 N. Vlachopoulos, P. Liska, J. Augustynski and M. Grätzel, *J. Am. Chem. Soc.*, 1988, **110**, 1216–1220.
80 S. R. Raga, E. M. Barea and F. Fabregat-Santiago, *J. Phys. Chem. Lett.*, 2012, **3**, 1629–1634.
81 D. P. Hagberg, T. Marinado, K. M. Karlsson, K. Nonomura, P. Quin, G. Boschloo, T. Brinck, A. Hagfeldt and L. Sun, *J. Org. Chem.*, 2007, **72**, 9550–9556.
82 S. Mohakud and S. K. Pati, *J. Mater. Chem.*, 2009, **19**, 4356–4361.
83 A. Datta, S. Mohakud and S. K. Pati, *J. Chem. Phys.*, 2007, **126**, 144710–144717.
84 M. P. Balany and D. H. Kim, *J. Mol. Struct.: THEOCHEM*, 2009, **910**, 20–26.
85 T. J. Meade, H. B. Gray and J. R. Winkler, *J. Am. Chem. Soc.*, 1989, **111**, 4353–4356.
86 L. Sicot, B. Geffroy, A. Lorin, P. Raimond, C. Sentein and J. M. Nunzi, *J. Appl. Phys.*, 2001, **90**, 1047–1054.
87 J. Preat, C. Michaux, D. Jacquemin and E. A. Perpete, *J. Phys. Chem. C*, 2009, **113**, 16821–16833.
88 M. Pastore, E. Mosconi, F. De Angelis and M. Gratzel, *J. Phys. Chem C*, 2010, **114**, 7205–7212.
89 T. Lu and F. Chen, *J. Comput. Chem.*, 2012, **33**, 580–592.